

Electron scale structures and magnetic reconnection signatures in the turbulent magnetosheath

E. Yordanova,¹ Z. Vörös,^{2,3,4} A. Varsani,² D. B. Graham,¹ C. Norgren,¹ Yu.

V. Khotyaintsev,¹ A. Vaivads,¹ E. Eriksson,¹ R. Nakamura,² P.-A.

Lindqvist,⁵ G. Marklund,⁵ R. E. Ergun,⁶ W. Magnes,² W. Baumjohann,² D.

Fischer,² F. Plaschke,² Y. Narita,² C.T. Russell,⁷ R.J. Strangeway,⁷ O. Le

Contel,⁸ C. Pollock,⁹ R.B. Torbert,¹⁰ B.J. Giles,⁹ J.L. Burch,¹⁰ L. A. Avanov⁹

J. C. Dorelli⁹ D. J. Gershman^{9,11} W. R. Paterson⁹ B. Lavraud^{12,13} Y. Saito¹⁴

Corresponding author: E. Yordanova, Swedish Institute of Space Physics, Box 537, SE-751 21

Uppsala, SWEDEN. (eya@irfu.se)

¹Swedish Institute of Space Physics,

Uppsala, Sweden.

²Space Research Institute, Austrian

Academy of Sciences, Graz, Austria.

³Department of Geophysics and Space

Sciences, Eötvös University, Hungary.

This article has been accepted for publication and undergone full peer review but has not been through the copyediting, typesetting, pagination and proofreading process, which may lead to differences between this version and the Version of Record. Please cite this article as doi: 10.1002/2016GL069191

⁴Geodetic and Geophysical Institute,
RCAES, Hungarian Academy of Sciences,
Sopron, Hungary

⁵Space and Plasma Group, Royal
Institute of Technology, Stockholm, Sweden.

⁶Laboratory of Atmospheric and Space
Physics, University of Boulder, USA.
⁷Institute of Geophysics and Planetary
Physics, University of California, Los
Angeles, USA.

⁸Laboratoire de Physique des Plasmas,
CNRS/Ecole Polytechnique/UPMC/Univ.
Paris Sud/Obs. de Paris, Paris, Paris-Sud,
France.

⁹NASA Goddard Space Flight Center,
Greenbelt, MD, USA.

¹⁰Southwest Research Institute, San
Antonio, USA.

¹¹Astronomy Department, University of
Maryland, College Park, MD, USA.

¹²IRAP, CNRS, Toulouse, France.

Collisionless space plasma turbulence can generate reconnecting thin current sheets as suggested by recent results of numerical magnetohydrodynamic simulations. The Magnetospheric Multiscale (MMS) mission provides the first serious opportunity to verify whether small ion-electron-scale reconnection, generated by turbulence, resembles the reconnection events frequently observed in the magnetotail or at the magnetopause. Here we investigate field and particle observations obtained by the MMS fleet in the turbulent terrestrial magnetosheath behind quasi-parallel bow shock geometry. We observe multiple small-scale current sheets during the event and present a detailed look of one of the detected structures. The emergence of thin current sheets can lead to electron scale structures. Within these structures, we see signatures of ion demagnetization, electron jets, electron heating and agyrotropy suggesting that MMS spacecraft observe reconnection at these scales.

Key Points

(Magnetic Reconnection, Turbulence)

¹³CNRS, UMR 5277, Toulouse, France

¹⁴JAXA, Japan.

1. Introduction

The main goal of Magnetospheric Multiscale (MMS) mission is the multi-point study of microphysics of magnetic reconnection (MR) targeting the structures within the electron diffusion region [Burch *et al.*, 2015, 2016]. Additional science goals include the understanding of the physics of particle acceleration and the clarification of the role of plasma turbulence in fast collisionless MR. On the other hand, high Reynolds number magnetohydrodynamic and PIC simulations show that turbulence can also generate spatially intermittent, thin and reconnecting current sheets [Greco *et al.*, 2008; Servidio *et al.*, 2009; Wan *et al.*, 2015]. The occurrence of MR in the turbulent terrestrial magnetosheath was also confirmed by Cluster measurements [Retinó *et al.*, 2007]. In turbulent space plasmas the ion-electron-scale current sheets are found to be associated with locally enhanced heating and energy dissipation [Osman *et al.*, 2012, 2014; Chasapis *et al.*, 2015]. Although in collisionless plasmas only approximate measures of energy dissipation can be introduced [Matthaeus *et al.*, 2015], the generation of spatially intermittent current sheets indicates that the associated kinetic dissipation, in which MR can play a crucial role, is spatially inhomogeneous. Despite the highly localized dissipation the heating of the plasma can be significant [Servidio *et al.*, 2012]. A recent experimental study based on Cluster data shows that turbulence generated thin proton-scale current sheets are ubiquitous in the magnetosheath downstream of a quasi-parallel bow shock [Vörös *et al.*, 2016]. This implies that turbulence may also generate numerous reconnecting current sheets which can be studied through high resolution field, plasma and particle measurements available from MMS. Secondary MR sites can also occur at MR generated flux ropes or in turbulent re-

connection exhausts [Lapenta *et al.*, 2015]. The large number of turbulence generated or secondary MR sites may substantially increase the probability of MMS encounter by the electron diffusion region. Global hybrid and fully kinetic simulations of the Earth's magnetosphere indicate that flux ropes and other plasma structures in the turbulent magnetosheath can also be generated by the interaction of the solar wind with the bow shock [Karimabadi *et al.*, 2014].

In this paper we investigate a possible MR site in the turbulent terrestrial magnetosheath by detailed analysis of field, plasma and particle observation by MMS space-craft. The different terms in the generalized Ohm's law are calculated and their relative contribution characterizing the ion and electron motion. Additionally, dimensionless proxies characterizing electron demagnetization and frozen flux violation are calculated from single point measurements [Zenitani *et al.*, 2011; Aunai *et al.*, 2013; Scudder *et al.*, 2015].

2. Data and instrumentation

The merged digital fluxgate (FGM) [Russell *et al.*, 2014] and search coil (SCM) [Le Contel *et al.*, 2014] data was developed by using instrument frequency and timing models that were created during the FIELDS integration test campaign [Torbert *et al.*, 2014]. These models are based on linear filter functions and can correct the respective frequency responses of the instruments in gain and phase. Using these models inflight data was corrected and data was added using low and high pass filter functions. Thus, the data set analyzed here consist of: data below 4Hz originating from FGM, data above - from SCM; and in the crossover region both data sets were used. A detailed description of the technique is due to appear in the specialized literature. The electric field data from EDP

instrument is available with time resolution of 8 kHz [Torbert *et al.*, 2014; Ergun *et al.*, 2014; Lindqvist *et al.*, 2014]. Ion and electron moments from FPI instrument [Pollock *et al.*, 2016] have time resolution 150 ms and 30 ms, respectively.

3. Event overview

On November 30, 2015 between 00:21 and 00:26 UT the MMS spacecraft were situated in the compressed turbulent magnetosheath, downstream of a quasi-parallel bow shock. At the same time, the solar wind monitors (OMNI database) observed an extended high-density compressional region at the leading edge of a high-speed stream, associated with a significant geomagnetic response (not shown). The overview plot (Figure 1) shows the observed field and plasma parameters between 00:26:03 and 00:26:18 UT. It is demonstrated here that this 15 sec long interval contains a flux rope and its interacting boundary/region comprising discontinuities, narrow current structures, and magnetic reconnection. These are the typical structures seen in simulations of plasma turbulence [Greco *et al.*, 2008; Servidio *et al.*, 2009; Wan *et al.*, 2015]. The subplots 1a – d show the total magnetic field B_{t_k} and magnetic components B_{x_k} , B_{y_k} and B_{z_k} in spacecraft reference frame. Indices k refer to MMS spacecraft. The so-called partial variance of increments (PVI), often used in studies of plasma turbulence to detect discontinuities and/or current sheets, has been here adapted to multi-spacecraft measurements [Chasapis *et al.*, 2015]. The signal PVI_{ij} has been calculated between spacecraft pairs i, j ($i, j = 1-4$ are the number of MMS spacecraft). PVI_{ij} are depicted in the subplot 1e, and are defined through:

$$PVI_{ij}(t) = \sqrt{\frac{|\Delta \mathbf{B}_{ij}(t)|^2}{\langle |\Delta \mathbf{B}_{ij}|^2 \rangle}}, \quad (1)$$

The latitude θ_2 and longitude ϕ_2 of magnetic field vector orientation for MMS 2 is shown in subplot 1*f*. Subplot 1*g* contains the pressures (total, dynamic, magnetic, ion thermal and electron thermal). Here the different pressure terms are shown with the same color for each spacecraft. The magnitudes of ion and electron speeds, \mathbf{V}_{ik} and \mathbf{V}_{ek} are shown in subplots 1*h* and 1*i*, respectively. The magnitudes of electric field \mathbf{E}_k in spacecraft reference frame and the magnitudes of current densities \mathbf{J}_k are shown in subplots 1*j* and 1*k*, respectively. \mathbf{J}_k 's are calculated for each spacecraft from plasma measurements through $\mathbf{J}_k = Nq(\mathbf{V}_{ik} - \mathbf{V}_{ek})$, where N is the plasma density and q is the charge of particles. The thick magenta line in subplot 1*k* corresponds to the magnitude of the current density \mathbf{J}_{curl} , estimated in the tetrahedron barycenter by using the curlometer technique [Dunlop *et al.*, 2002]. The cyan curve, noted as \mathbf{J}_{plasma} in the same subplot is the average plasma current over the four spacecraft. Its comparison with the current obtained from the curlometer demonstrates the very good agreement in the current estimation by the two approaches.

There exist two different physical regions which can be identified in Figure 1. A twisted flux rope extends roughly from 00:26:10 UT to the end of the time interval. It can be identified on the basis of the slow rotation and sign-change of the magnetic field, seen in B_{zk} (subplot 1*d*), changing from -32 nT (minimum) to +8 nT (maximum). The slow rotation is also seen in θ_2 . Other signatures of the flux rope include the maxima of Bt_k (subplot 1*a*) and total pressure P_{tot} (subplot 1*g*) between 00:26:11 and 00:26:13 UT. Although the ion P_{therm} is higher than P_{mag} , the profile of P_{tot} having maximum near the rope axis [Zaqarashvili *et al.*, 2014] is determined by P_{mag} . To support the flux rope identification, we have calculated the dot product between \mathbf{J}_{curl} and \mathbf{B} . If a helical flux

rope is carrying a current, this current should be roughly along \mathbf{B} , therefore $\mathbf{J}_{curl} \cdot \mathbf{B} \neq 0$, as it has been verified for our case (not shown).

At the left border of the flux rope (roughly between 00:26:05 and 00:26:10 UT) we observe a distinct feature in all parameters. Further in the paper we will refer to it as the region of interest. Within this region the differences between magnetic field values (subplots 1a – d) become larger, indicating increased magnetic gradients. PVI_{ij} show the occurrence of two discontinuities (subplot 1e), where also the orientations of magnetic vectors (θ and ϕ in subplot 1f) exhibit sudden changes. At the same time, there exist significant changes and narrow peaks in Ve_k , E_k and J_k , while the Vi_k variations are much smaller, indicating the occurrence of differential motion between ions and electrons at narrow structures. The electron inertial length in this region is ~ 0.7 km and the Doppler shifted frequency associated with this scale corresponds to about 26 Hz. These structures are narrower than the inter-spacecraft separation (~ 10 km), therefore the curlometer cannot detect them (the magenta curve of J_{curl} is much smoother in subplot 1k). The narrow peaks in \mathbf{Ve}_k , \mathbf{E}_k and \mathbf{J}_k between 00:26:08.5 and 00:26:10 UT are subsequently seen by all spacecraft, therefore representing real spatial structures.

4. The event in a new coordinate system

To better understand the event presented in Figure 1 the physical variables were rotated to the field-aligned coordinate system, in which X: \mathbf{B} , Y: $\mathbf{E} \times \mathbf{B}$ and Z: $\mathbf{B} \times \mathbf{E} \times \mathbf{B}$. We have chosen a rotation matrix at the instant of electron speed maximum before 00:26:10 UT in Figure 2 (subplot 2d), which served as a global coordinate system for the whole event. In this coordinate system the largest variations of the magnetic field occur at the border of the

flux rope in B_x and B_z components, while B_y is changing slowly (subplots 2a–c). The flux rope interval after 00:26:10 UT is characterized by a slow rotation of the magnetic field. The electron speed components (subplots 2d – f) show occurrence of jets at the border, while the ion speed increase is smaller and the variation is smoother (subplots 2g – j). Similar electron jets have been observed at the magnetopause [Khotyaintsev, *et al.*, 2016, this issue]. The ion and electron Alfvén speeds vary between spacecraft from 115 to 125 km/s. Electron and proton parallel and perpendicular temperatures are shown in subplots 2i and k. $T_{e\parallel}$ (subplot 2i) shows two peaks associated with temperature anisotropy and parallel electron heating at the left and right borders of the region between 00:26:05 and 00:26:11 UT in all spacecraft. Similar increases have been observed by recent MMS measurements at the magnetopause near the diffusion region and have been interpreted as evidence for a potential reconnection exhaust [Graham *et al.*, 2016; Lavraud *et al.*, 2016]. The ion temperature anisotropy however, is absent within this region (subplot 2k). The slight increase of ion plasma density (subplot 2l) together with the increase of magnetic field (subplot 2a) and total/magnetic pressure (Figure 1g) between 00:26:09 and 00:26:11 UT indicates that this is a compressional region. The fluctuations and temperature anisotropies after 00:26:11 UT are associated with the flux rope again.

5. Generalized Ohm's law terms

In collisionless plasmas magnetic reconnection represents a multi-scale process where characteristic reconnection structures over different scales can be observed. It is described by the generalized Ohm's law been written in terms of the electric field \mathbf{E} [Khotyaintsev *et al.*, 2006]:

$$\mathbf{E} + \mathbf{V}_i \times \mathbf{B} = \frac{\mathbf{J} \times \mathbf{B}}{ne} + \frac{\nabla \cdot \mathbf{P}_e}{ne} \quad (2)$$

where the electron inertia terms are neglected, \mathbf{V} is the plasma bulk flow speed, \mathbf{J} is the current density, \mathbf{P}_e is the electron pressure tensor, \mathbf{E} is the electric field in spacecraft frame, \mathbf{B} is the magnetic field, m_e is the electron mass, n is the number density, and e is the proton charge. All quantities have been transformed in the new coordinate system described in the previous section. The z (out-of-plane) components of the terms in the generalized Ohm's law and their relative strength indicate if the spacecraft are crossing the ion or electron diffusion regions [Nakamura *et al.*, 2016]. The different terms in the Ohm's law are plotted in Figure 3 *a – e*. The $(\mathbf{V}_i \times \mathbf{B})_z$ is small (subplot 3*a*), however, the electric field in the electron frame $(\mathbf{E} + \mathbf{V}_e \times \mathbf{B})_z$ is large around 00:26:10 UT (subplot 3*b*).

The Hall term $(\mathbf{J} \times \mathbf{B}/ne)_z$ in subplot 3*c* indicates that $(\mathbf{V}_e \times \mathbf{B})_z \gg (\mathbf{V}_i \times \mathbf{B})_z$ and the differential motion of electrons and ions leads to significant Hall terms. The $\mathbf{E} \cdot \mathbf{J}$ reaching large values in the region of interest (subplot 3*d*) indicates that electromagnetic energy is converted to thermal and kinetic energies.

Additionally, Figure 3*f* shows the \sqrt{Q} parameter introduced by [Swisdak, 2016] representing a measure of gyrotropy of the electron pressure tensor. It is defined as following:

$$Q = 1 - \frac{4I_2}{(I_1 - P_{\parallel})(I_1 + 3P_{\parallel})}, \quad (3)$$

where $I_1 = P_{xx} + P_{yy} + P_{zz}$, $I_2 = P_{xx}P_{yy} + P_{xx}P_{zz} + P_{yy}P_{zz} - (P_{xy}P_{yx} + P_{xz}P_{zx} + P_{yz}P_{zy})$, and $P_{\parallel} = \hat{\mathbf{b}} \cdot \mathbf{P} \cdot \hat{\mathbf{b}}$. Note, that linear changes are assumed over the spacecraft tetrahedron in the electron pressure calculation, thus shorter than spacecraft separation length scales could be underestimated [Paschmann *et al.*, 2000]. For gyrotropic tensors $Q=0$, while

maximal agyrotropy is reached at $Q=1$. The variations due to electron pressure tensor, $(\nabla \cdot \mathbf{P}_e/ne)_z$ (subplot 3e) are also elevated when the electric field in the electron frame (subplot 3b) is high. Similar behavior is observed at the magnetopause [Norgren *et al.*, 2016, this issue]. Finally, according to PIC simulations [Swisdak, 2016] the parameter \sqrt{Q} reaching values about 0.05 indicates significant agyrotropy, which occurs near the separatrices or reconnection X-lines. This is most pronounced at about 00:26:09.5 UT for MMS 1 (black peak in subplot 3f), note however that \sqrt{Q} is enhanced within the whole interaction region.

6. Particle distributions

Figure 4, represents the plasma observations by FPI ion and electron instrument on MMS 1. The top four horizontal panels are the timeseries energy spectrograms of the ions and electrons. Ion distribution perpendicular to the local magnetic field is shown in subplot 4a. The electrons three distributions: parallel, perpendicular and anti-parallel to the magnetic field are presented in subplots 4b – d, respectively. From the ion energy spectrogram (subplot 4a), it is evident that at 00:26:00 UT the ion population has an energy centered at ~ 750 eV. After that the flux of ions shows some variations, however the center of energy remains the same. The first clear change occurs at $\sim 00:26:07.5$ UT around the time that total magnetic field reaches its minimum value, where the flux of ions is also increased. Then at $\sim 00:26:09.6$ UT, a distinct colder population with energies centered at ~ 150 eV emerges, whilst a lower flux population is also centered at ~ 400 eV. The colder magnetosheath ions are observed until $\sim 00:26:10.5$ UT where a higher energy population, narrowly distributed around ~ 500 eV, appears. The latter is the dominant

population until 00:26:14.2 UT, when ions are separated in two distinct populations, one centered at ~ 300 eV and the other at 1 KeV. This trend continues until the end of the period at 00:26:20 UT, where the ions have one population with $\sim 700 - 800$ eV energy.

The energy spectrogram of the electrons shows that at the start of the period, they are mainly bistreaming (subplots 4*b*, 4*d*), which continues until $\sim 00:26:03.4$ UT when the distribution becomes rather isotropic. At $\sim 00:26:07.1$ UT, the distribution turns to bistreaming for a short period (about ~ 0.5 second) before the minima of the total magnetic field. The population is again isotropic until $\sim 00:26:09.6$ UT when the magnetic field $B_z = 0$. At this time, the population is predominantly anti-field aligned, resulting in the velocity of electrons reaching ~ 600 km/s purely in that direction. This narrow region quickly passes by MMS 1, and only 0.2 second later, the electrons are observed to be moving mainly perpendicular to the magnetic field (subplot 4*c*) with speed of ~ 550 km/s, which lasted ~ 0.1 second. In this short interval the center of energy for the electrons quickly rise from ~ 100 eV to ~ 150 eV and then back to ~ 100 eV. This time interval, which is marked by the rectangle in Figure 4, is when the values of \sqrt{Q} reach their maximum, representing a non-gyrotropy in electron distribution. In addition to that, this signature is also accompanied with appearance of colder ion population as mentioned above (subplot 4*a*), and therefore is of particular interest. After this time, the perpendicular electrons (subplot 4*c*) show variations at 00:26:10.6, 11.9, 12.9, 14.1 and 16.1 UT, whilst the parallel and antiparallel stay relatively equal (subplots 4*b*, 4*d*). However, between 00:26:09.6 and 00:26:09.8 UT, it is the only time interval that the

maximum velocity (Fig. 1*i*) and a clear increase in the flux of electrons are observed (Fig. 4*b, c*).

Figure 4*e–h* show the Velocity Distribution Function (VDF) of particles for a snapshot at 00:26:09.710 and 00:26:09.800 UT. The upper and bottom pair of panels are cuts of VDFs for electrons (4*e, f*) and ions (4*g, h*) in $\mathbf{V}_{\parallel}-\mathbf{V}_{\perp_1}$ and $\mathbf{V}_{\perp_1}-\mathbf{V}_{\perp_2}$ diagrams, where \mathbf{V}_{\parallel} represents the velocity along the magnetic field orientation, \mathbf{V}_{\perp_1} and \mathbf{V}_{\perp_2} respectively along $(\mathbf{E} \times \mathbf{B})$ and $\mathbf{B} \times (\mathbf{E} \times \mathbf{B})$ directions. The $\mathbf{V}_{\parallel}-\mathbf{V}_{\perp_1}$ plot for the electrons (subplot 4*e*) shows that, while the lowest energy population are approximately isotropic, there is also a population which were purely moving in positive $(\mathbf{E} \times \mathbf{B})$ direction. The former population as also mentioned above is ~ 100 eV and the later ~ 150 eV. The simultaneous observations of ions however show that the main population (~ 400 eV) is anti-field aligned, whilst there is no clear $(\mathbf{E} \times \mathbf{B})$ drifted population.

In the $\mathbf{V}_{\perp_1}-\mathbf{V}_{\perp_2}$ plot for the electrons (subplot 4*f*), the population with lowest energy (< 100 eV) is gyrotropic, but the higher energy (~ 150 eV) population show a clear non-gyrotropy with the electrons being shifted in positive $(\mathbf{E} \times \mathbf{B})$ direction. In a $(\mathbf{E} \times \mathbf{B})$ drifted distribution in plasma, it is expected that the lower energy particles are more effected due to the relative velocity drift. However for this case, the fact that the lower energy population is drifted less than the higher energy population, it may suggest that the latter is a distinct population. The simultaneous VDF for ions (subplots 4*g, h*) shows that the highest flux ions are predominantly moving in negative direction of $\mathbf{B} \times (\mathbf{E} \times \mathbf{B})$ directions (subplot 4*h*). This population is the same cold ions centered at ~ 150 eV (subplot 4*a*), which emerged at the time of the rotation of B_z component in the magnetic field (Fig. 1*d*).

. Also the lower flux ions with energy centered at ~ 400 eV, are approximately gyrotropic at this time (Fig. 4a) .

7. Discussion and summary

The appearance of the two distinct cold and hot populations of ions leading to a non-maxwellian distribution, suggests that these observations have taken place where ions were demagnetized. (e.g. [Dai *et al.*, 2015; Zhou *et al.*, 2009]). This idea is supported by the non-gyrotropic shape of the ion distributions in VDF plots (Fig. 4g, h), where an asymmetric reconnection (e.g. [Lee *et al.*, 2014]) can lead to mixing up distinct sources of plasma with different energies. The separation of two populations in \mathbf{V}_{\perp_1} - \mathbf{V}_{\perp_2} plane along (Fig. 4h) is also consistent with previous observations of ion diffusion region by [Dai *et al.*, 2015] using THEMIS spacecraft.

At electron scale, the narrow region with excessive anti-field aligned electron jet, followed by a jet along ($\mathbf{E} \times \mathbf{B}$) direction in the interval where \mathbf{E} field reached its maximum, suggests a possible passage of the spacecraft near the X-line. Similar signatures of diffused ions followed by electron outflow with electrons frozen-in on the reconnected field line have been observed in the separatrix region in simulation of asymmetric reconnection at the magnetopause [Khotyaintsev *et al.*, 2016, and Shay *et al.*, 2016, this issue]. There is also an increase in the agyrotropy parameter Q for the electrons, which is expected to be seen around the electron diffusion region, however the observations are not accompanied with a crescent shaped distribution of electrons in \mathbf{V}_{\perp_1} - \mathbf{V}_{\perp_2} plane (e.g [Hesse *et al.*, 1999, 2011]).

Note that this crescent shape is clearer for magnetopause reconnection where the two sources of plasma have clear energy differences, whilst in the magnetosheath, similarly to

the magnetotail [Henderson *et al.*, 2006], it may not be the case. Overall, the particle data here suggest that most of the observations are near the X-line inside ion diffusion region. The spacecraft does not clearly enter the electron diffusion region, however the non-diagonal elements of electron pressure tensor increase significantly as MMS 1 probably crossed the separatrix region. This is consistent with simulations on the spatial dimensions of the electron diffusion region (e.g. [Nakamura *et al.*, 2016; Swisdak, 2016]).

In summary, the main motivation for this study is to show that coherent structures such as flux ropes, current sheets, reconnection associated multi-scale structures, can be observed over proton and electron scales in the turbulent magnetosheath by MMS spacecraft. The analyzed time interval comprised a flux rope with slightly rotating magnetic field with compressions, discontinuities, current sheets, electron and ion scale ($\sim 0.5\text{-}30$ km) structures developing at its border. In this region of interest, the four MMS spacecraft observed: 1) strong electron scale currents; 2) significant z components of the electric field in the electron frame $(\mathbf{E} + \mathbf{V}_e \times \mathbf{B})_z$ and the Hall term $(\mathbf{J} \times \mathbf{B}/ne)_z$; 3) signature of demagnetized ions and ion Alfvén outflow; 4) fast electron jets; 5) electron heating; 6) $\mathbf{E} \cdot \mathbf{J}$ up to ~ 70 nW/m^3 at narrow peaks indicating that the electromagnetic energy is converted and dissipated; and 6) electron pressure agyrotropy. These features suggest that MMS observes MR site within electron scale current sheets in the turbulent magnetosheath plasma.

This study, complementing and further developing the ideas about turbulence generated structures by observations in the magnetosheath [Retinó *et al.*, 2007; Chasapis *et al.*, 2015; Vörös *et al.*, 2016] and in the solar wind [Greco *et al.*, 2016]; and by simulations

[Karimabadi *et al.*, 2013], suggests that electron scale structures and reconnecting current sheets may occur not only at the large-scale boundaries, such as the magnetopause or magnetotail current sheet, but also in turbulent collisionless plasmas. We believe that these findings might encourage more thorough investigations of turbulence generated structures by using the high resolution measurements of MMS.

Acknowledgments. E.Y. and Z. V. research leading to these results has received funding from the European Community's Seventh Framework Programme ([7/2007–2013] under grant agreement n°313038/STORM. Z.V. was supported by the Austrian Fond zur Förderung der wissenschaftlichen Forschung (project P24740-N27). IRAP contribution and the French involvement to (SCM) on MMS are supported by CNES and CNRS. Y.K. and D.B.G. were supported by the Swedish National Space Board, grants 139/12 and 175/15. Parts of the particle plots presented in this paper are generated using the QSAS software.

References

- Aunai, N., M. Hesse, and M. Kuznetsova (2013) Electron nongyrotropy in the context of collisionless magnetic reconnection, *Phys. Plasmas*, 20, 092903.
- Burch, J.L., T. E. Moore, R. B. Torbert, and B.L. Giles (2015) Magnetospheric Multiscale Overview and Science Objectives, *Space Sci. Rev.*, doi:10.1007/s11214-015-0164-9
- Burch, J. L., R. B. Torbert, T. D. Phan, L.-J. Chen, T. E. Moore, R. E. Ergun, J. P. Eastwood, D. J. Gershman, P. A. Cassak, et al. (2016) Electron-Scale Measurements of Magnetic Reconnection in Space, *Science*, in press, doi:10.1126/science.aaf2939

Chasapis, A., A. Retinó, F. Sahraoui, A. Vaivads, Yu. V. Khotyaintsev, et al. (2015) Thin Current Sheets and Associated Electron Heating in Turbulent Space Plasma, *Astrophys. J. Lett.*, 804, L1.

Dai, L., Wang, C., Angelopoulos, V., and Glassmeier, K.-H., (2015) In situ evidence of breaking the ion frozen-in condition via the non-gyrotropic pressure effect in magnetic reconnection, *Ann. Geophys.*, 33, 1147–1153.

Dunlop, M. W., Balogh, A., Glassmeier, K.-H., and P., Robert, (2002) Four-point Cluster application of magnetic field analysis tools: The Curlometer, *J. Geophys. Res.*, 107, A11, SMP 23-1.

Ergun, R. E.; Tucker, S.; Westfall, J.; Goodrich, K. A.; Malaspina, D. M.; Summers, D.; Wallace, J.; Karlsson, M., et al. (2014) The Axial Double Probe and Fields Signal Processing for the MMS Mission, *Space Sci. Rev.*, 107, 10.1007/s11214-014-0115-x.

Greco, A., P. Chuchai, W. H. Matthaeus, S. Servidio, and P. Dmitruk (2008) Intermittent MHD structures and classical discontinuities, *Geophys. Res. Lett.*, 35, L19111.

Greco, A., S. Perri, S. Servidio, E. Yordanova, and P. Veltri (2016) The Complex Structure of Magnetic Field Discontinuities in the Turbulent Solar Wind, *Astrophys. J. Lett.*, accepted.

Graham, D. B., Yu. V. Khotyaintsev, C. Norgren, A. Vaivads, M. André, P.-A. Lindqvist, G. T. Marklund, R. E. Ergun, W. R. Paterson, et al. (2016) Electron currents and heating in the ion diffusion region of asymmetric reconnection, *Geophys. Res. Lett.*, 43, doi:10.1002/2016GL068613.

Henderson, P. D., C. J. Owen, A. D. Lahiff, I. V. Alexeev, A. N. Fazakerley, E. Lucek, and H. Réme (2006), Cluster PEACE observations of electron pressure tensor divergence in the magnetotail, *Geophys. Res. Lett.*, *33*, L22106.

Hesse, M., Schindler, K., Birn, J., and M. Kuznetsova (1999) The diffusion region in collisionless magnetic reconnection, *Phys. Plasmas*, *6*, 1781-1795.

Hesse, M., Neukirch, T., Schindler, K., Kuznetsova, M., and S., Zenitani (2011) The Diffusion Region in Collisionless Magnetic Reconnection, *Space Sci. Rev.*, *160*, 3-23.

Karimabadi, H., V. Roytershteyn, H. X. Vu, Y.A. Omelchenko, J. Scudder, et al. (2014) The link between shocks, turbulence, and magnetic reconnection in collisionless plasmas, *Phys. Plasmas*, *21*, 062308-1 – 062308-21.

Karimabadi, H., V. Roytershteyn, M. Wan, W.-H. Matthaeus, W. Daughton, et al. (2013) Coherent structures, intermittent turbulence, and dissipation in high temperature plasmas, *Phys. Plasmas*, *20*, 012303.

Khotyaintsev, Yu. V., Vaivads, A., Retin, A., Andr, M., Owen, C. J., and H. Nilsson (2006) Formation of Inner Structure of a Reconnection Separatrix Region, *Phys. Rev. Lett.*, *97*, 205003.

Khotyaintsev, Yu. V., D. B. Graham, C. Norgren, E. Eriksson, W. Li, A. Johlander, A. Vaivads, M. André, P. L. Pritchett, A. Retino, et al. (2016) Electron jet of asymmetric reconnection, *Geophys. Res. Lett.*, *43*, doi:10.1002/2016GL069064.

Lavraud, B., et al. (2016) Currents and associated electron scattering and bouncing near the diffusion region at Earths magnetopause, *Geophys. Res. Lett.*, *43*, doi:10.1002/2016GL068359.

Lapenta, G. , S. Markidis, M. V. Goldman, and D. L., Newman (2015) Secondary reconnection sites in reconnection-generated flux ropes and reconnection fronts, *Nature Physics*, 11, 690-695.

Le Contel, O., P. Leroy, A. Roux, C. Coillot, D. Alison, A. Bouabdellah, et al. (2014) The Search-Coil Magnetometer for MMS, *Space Sci. Rev.*, doi: 10.1007/s11214-014-0096-9.

Lee, S. H., Zhang, H., Zong, Q.-G., Otto, A., Sibeck, D. G., Wang, Y., Glassmeier, K.-H., Daly, P. W., and H., Rme (2014) Plasma and energetic particle behaviors during asymmetric magnetic reconnection at the magnetopause, *J. Geophys. Res.-Space*, 119, 1658-1672.

Lindqvist, P.-A., Olsson, G., Torbert, R. B., King, B., Granoff, M., Rau, D., Needell, G., Turco, S., Dors, I., et al. (2014) The Spin-Plane Double Probe Electric Field Instrument for MMS, *Space Sci. Rev.*, doi:10.1007/s11214-014-0116-9.

Matthaeus,W. H., M. Wan, S. Servidio, A. Greco, K. T. Osman, S. Oughton, and P. Dmitruk (2015) Intermittency, nonlinear dynamics and dissipation in the solar wind and astrophysical plasmas, *Phil. Trans. R. Soc. A*, 373, 20140154.

Nakamura,T., R. Nakamura, and H. Hasegawa (2016) Spatial dimensions of the electron diffusion region in anti-parallel magnetic reconnection, *Ann. Geophys.*, 34, 357–367.

Osman, K. T.,W. H. Matthaeus, M. Wan, and A. F. Rappazzo (2012) Intermittency and Local Heating in the Solar Wind, *Phys. Rev. Lett.*, 108, 261102.

Osman, K. T.,W. H. Matthaeus, J. T. Gosling, A. Greco, S. Servidio, B. Hnat, et al. (2014) Magnetic Reconnection and Intermittent Turbulence in the Solar Wind, *Phys. Rev. Lett.*, 112, 215002.

Paschmann, G. and Schwartz, S. J. (2000) ISSI Book on Analysis Methods for Multi-Spacecraft Data, *ESA Special Publication*, 449.

Pollock, C., T. Moore, A. Jacques, J. Burch, U. Gliese, Y. Saito, et al. (2016) Fast Plasma Investigation for Magnetospheric Multiscale, *Space Sci. Rev.*, 1–76, doi:10.1007/s11214-016-0245-4.

Retinò, A., D. Sundkvist, A. Vaivads, F. Mozer, M. André, and C. J. Owen (2007) In situ evidence of magnetic reconnection in turbulent plasma, *Nature Physics*, 3, 236–238.

Russell, C. T., B. J. Anderson, W. Baumjohann, K. R. Bromund, D. Dearborn, D. Fischer, et al. (2014) The Magnetospheric Multiscale Magnetometers, *Space Sci. Rev.*, doi:10.1007/s11214-014-0057-3.

Scudder, J.D., H. Karimabadi, W. Daughton, and V. Roytershteyn (2015) Frozen flux violation, electron demagnetization and magnetic reconnection, *Phys. Plasmas*, 22, 101204-1-101204-22.

Servidio, S., W. H. Matthaeus, M. A. Shay, P. A. Cassak, and P. Dmitruk (2009) Magnetic reconnection and two-dimensional magnetohydrodynamic turbulence, *Phys. Rev. Lett.*, 102, 115003-1-115003-4.

Servidio, S., F. Valentini, F. Califano, and P. Veltri (2012) Local Kinetic Effects in Two-Dimensional Plasma Turbulence, *Phys. Rev. Lett.*, 108, 045001.

Shay, M. A., T. D. Phan, C. C. Haggerty, M. Fujimoto, J. F. Drake, K. Malakit, P. A. Cassak, and M. Swisdak (2016), Kinetic signatures of the region surrounding the X-line in asymmetric (magnetopause) reconnection, *Geophys. Res. Lett.*, 43, doi:10.1002/2016GL069034.

Swisdak, M. (2016) Quantifying gyrotropy in magnetic reconnection, *Geophys. Res. Lett.*, 43, 43–49.

Torbert, R. B., C. T. Russell, W. Magnes, R. E. Ergun, P.-A. Lindqvist, O. LeContel, et al. (2014) The FIELDS Instrument Suite on MMS: Scientific Objectives, Measurements, and Data Products, *Space Sci. Rev.*, doi: 10.1007/s11214-014-0109-8.

Vasyliunas, T. M. (1975) Theoretical models of magnetic field line merging. I, *Reviews of Geophysics and Space Physics*, 13, 303–336.

Vörös, Z., E. Yordanova, M.M. Echim, G. Consolini, and Y. Narita (2016) Turbulence-generated proton-scale structures in the terrestrial magnetosheath, *Astrophys. J. Lett.*, 819: L15.

Wan, M., W. H. Matthaeus, V. Roytershteyn, H. Karimabadi, T. Parashar, P. Wu, and M. Shay (2015) Intermittent dissipation and heating in 3D kinetic plasma turbulence, *Phys. Rev. Lett.*, 114, 175002-1-175002-5.

Zaqarashvili, T., Z. Vörös, Narita, and R. Bruno (2014) Twisted magnetic flux tubes in the solar wind, *Astrophys. J. Lett.*, 783: L19.

Zenitani, S., M. Hesse, A. Klimas, and M. Kuznetsova (2011) New Measure of the Dissipation Region in Collisionless Magnetic Reconnection, *Phys. Rev. Lett.*, 106, 195003.

Zhou, X.-Z., Angelopoulos, V., Runov, A., Sitnov, M. I., Zong, Q.-G., and Z. Y. Pu (2009) Ion distributions near the reconnection sites: Comparison between simulations and THEMIS observations, *J. Geophys. Res.-Space*, 114, A12211.

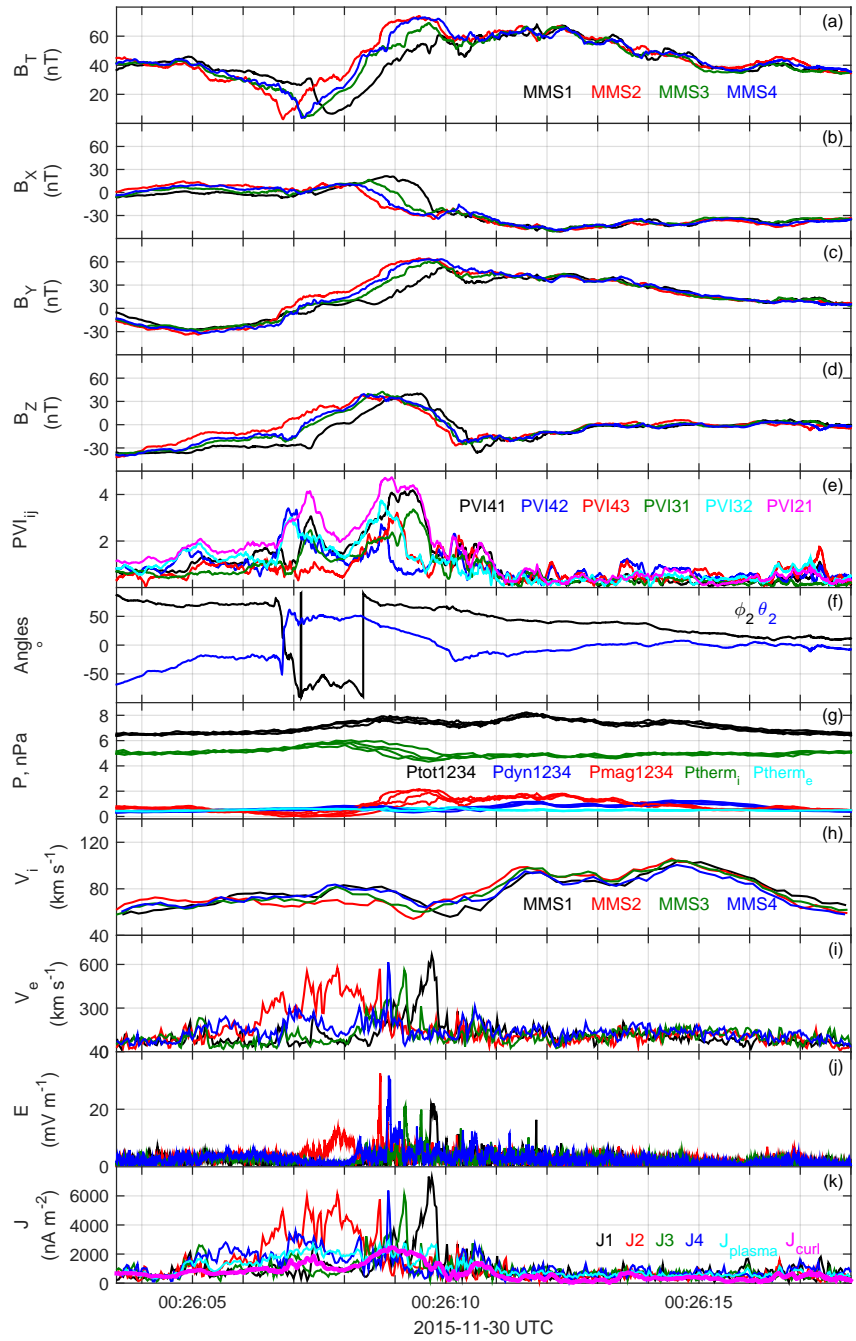


Figure 1. Field and plasma parameters in spacecraft coordinates: a) Magnetic field magnitude for the four MMS spacecraft (color coded); b) - d) magnetic field components; e) PVI_{ij} from pairs of spacecraft ($i,j = \text{MMS 1 - 4}$); f) the elevation and azimuthal angle of the magnetic field for MMS 2; g) Pressure for all spacecraft: total (black), dynamical (blue), magnetic (red), ion thermal (green), and electron thermal (cyan); h) ion velocity for all spacecraft; i) electron velocity; j) electric field magnitude; and k) electric current from plasma for each spacecraft, the averaged over all spacecraft plasma current (cyan) and the current from curlometer (magenta).

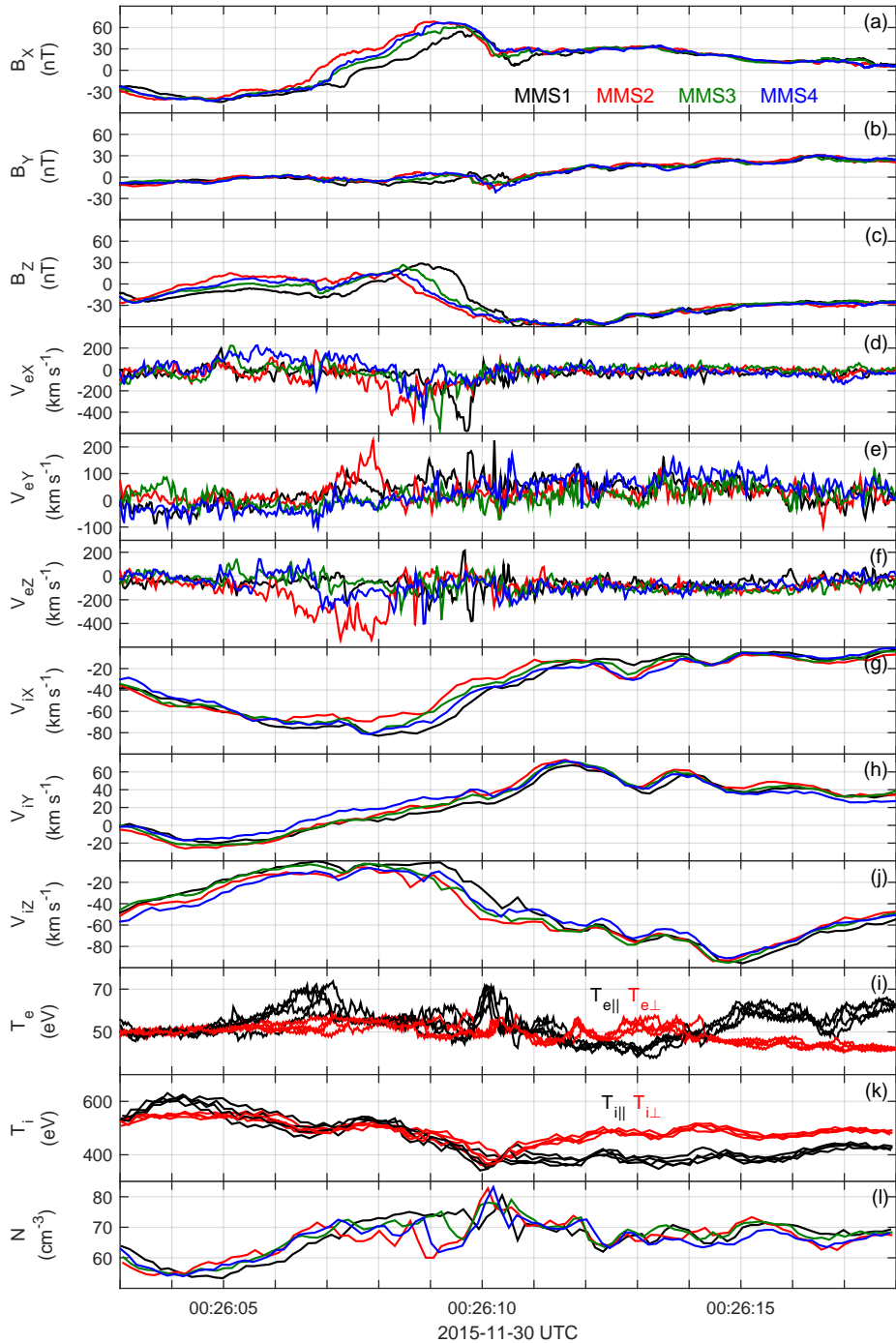


Figure 2. Field and plasma parameters in the rotated coordinate system: a) - c) magnetic field components for all spacecraft; d) - f) electron speed components; g) - j) ion speed components; i) - k) parallel (black) and perpendicular (red) to the background magnetic field electron and ion temperature for all spacecraft, respectively; and l) ion density.

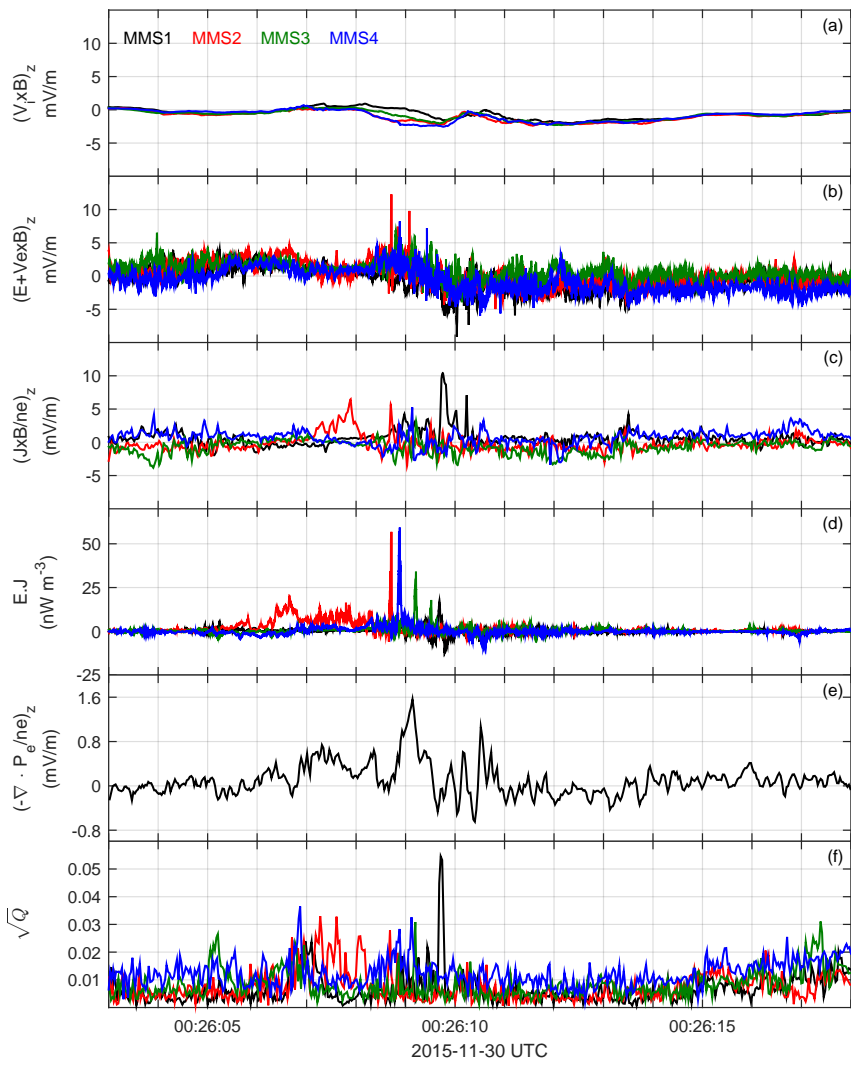


Figure 3. Generalized Ohm's law terms: a) ion convection component in Z-direction; b) z-component of the electric field in electron frame; c) Hall term component in Z-direction; d) E.J dissipation; e) electron pressure term in Z; and f) agyrotropy parameter.

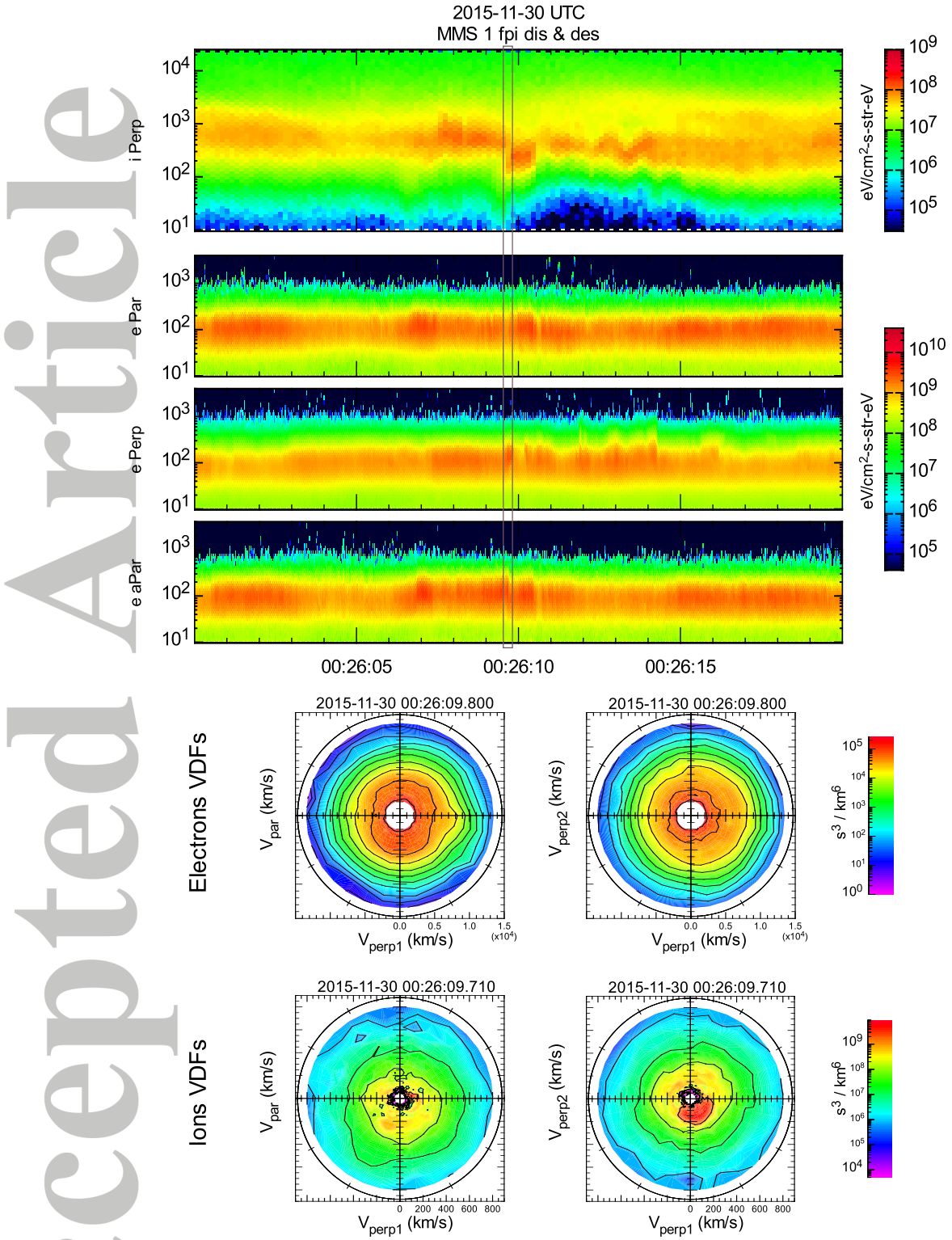


Figure 4. Particle energy spectrograms: a) ion distribution perpendicular to the local magnetic field; b) - d) electron distribution respectively parallel, perpendicular and anti-parallel to the magnetic field. Velocity Distribution Functions (VDFs) cuts for electrons in directions: e) $\mathbf{V}_{\perp 1}$ vs \mathbf{V}_{\parallel} , and f) $\mathbf{V}_{\perp 1}$ vs $\mathbf{V}_{\perp 2}$; g) and h) the same VDFs cuts for ions.